Journal of Power Sources 521 (2022) 230957

Contents lists available at ScienceDirect

Journal of Power Sources

journal homepage: www.elsevier.com/locate/jpowsour

Real-time monitoring of internal structural deformation and thermal events in lithium-ion cell via embedded distributed optical fibre

Yifei Yu [a,*], Elena Vergori [b], Faduma Maddar [a], Yue Guo [c], David Greenwood [a], James Marco [a]

[a] Energy Innovation Centre, Warwick Manufacturing Group, University of Warwick, Coventry, CV47AL, United Kingdom
[b] Politecnico di Torino – Dipartimento di Ingegneria Meccanica e Aerospaziale, Corso Duca degli Abruzzi, Torino, Italy
[c] Institute for Future Transport and Cities, Coventry University, Coventry, CV1 5FB, United Kingdom

HIGHLIGHTS

- Novel characterisation of electrode materials.
- Distributed fibre sensors embedded in LIBs for thermal and structural monitoring.
- Operando tracking of the SEI formation and the irreversible anode strain.
- In-depth assessment of anode structural deformation together with SOC and SOH.
- To optimise of future battery designs and to promote LIB safety improvement.

ARTICLE INFO

Keywords:
Li-ion batteries
Distributed and embedded sensors
Anode structural and thermal monitoring
Fibre optics

ABSTRACT

The in-operando monitoring of the cell's kinetic thermal and electrochemical processes during operation is a key requirement to understand battery performance, improve safety and to extend battery life. This research presents *in-situ* measurements of strain and temperature evolution within a graphite electrode during electromechanical lithiation and delithiation. By embedding distributed fibre optics sensor, the frequency shift associated with both temperature and strain are decoupled, allowing the real-time measurement of the solid electrolyte interface formation and the structural deformation within the anode. An in-depth assessment of electrode strain as a function of State of Charge (SoC) and State of Health (SoH) from the formation cycle through to electrical loading allows the assessment of cell performance over its complete life. It is observed that irreversible and non-uniformly distributed anode structural deformation was measured during the formation. The anode reveals an extensive mechanical strain increase with a coefficient of 0.96 με/SoC(%) with respect to the SoC and undergoes a compressive mechanical strain as SoH decreases from 100% to 47%. Collectively, the findings presented provide valuable new information to understand the causes of battery performance degradation as a result of electrode strain and temperature, underpinning new opportunities for battery characterisation and optimal system design.

1. Introduction

Lithium ion battery (LIB) technologies of various chemistries and forms have played a central role in the energy storage industry, from everyday consumer products to hybrid/electric vehicles and grid storage. Their unique combined characteristics, which include: high energy and power densities, cost, safety and cycle life, have made such technologies the default choice for many manufactures. As a result, understanding overall cell performance is crucial throughout the life of the LIB is of significant importance. Traditional battery cells are passive sources of energy and power where relatively few parameters, including terminal voltage, current, and surface temperature, are measured and therefore the understanding of cell operation is often limited. A better understanding and real-time monitoring of internal cell kinetics, observing the electrochemical and thermal states of the internal components via smart sensing functionalities is of critical need [1,2]. This will provide a holistic new insight and will contribute in the development of improved battery designs, the creation of new models that aim

* Corresponding author.
E-mail address: Yifei.Yu.1@warwick.ac.uk (Y. Yu).

https://doi.org/10.1016/j.jpowsour.2021.230957
Received 6 September 2021; Received in revised form 10 December 2021; Accepted 23 December 2021
Available online 29 December 2021

to represent the LIB at the electrode or microstructure scale [1,3,4] and the design of new algorithms for the battery management system (BMS) to monitor LIB performance and extend life [5,6].

Cycling performance of a LIB depends on a wide range of processes including chemical and electrochemical reactions, phase change reactions and ionic transport, promoting strain in electrode particles and changes in electrode volume [7–9]. This impacts the nature and kinetics of the internal interfaces that govern cell lifetime and performance [10]. In LIBs, lithium ions shuttle between the positive and negative electrodes upon charging and discharging. Intercalation of lithium ions into graphite results in the expansion of its crystallographic lattice, and the associated microscopic stress is seen, by many researchers, to be the intrinsic driving force for anode swelling [11]. Such swelling phenomena have detrimental effects on a battery's cycle life [9,12]. Additionally, with its uncontrolled rate and inefficient formation, cell swelling may lead to increased heat generation [13–15]. The heat is generated internally, leading to thermal gradient induced position-dependant aging, such as non-uniform resistance and solid electrolyte interface (SEI) growth [16]. For a pouch cell application, the stress on the anode could result in undesirable volume expansion, which must be managed within the design of the complete battery system and result in further complexities for LIB packaging and thermal management [17]. Further to improve performance monitoring, the operando monitoring of internal thermal and mechanical variation can provide an early indication of the onset of cell failure, establishing a correlation between microstructural characteristics and electrochemistry is thus important for providing an indication of the root causes of the general measures of State-of-Charge (SoC) and State of Health (SoH). Therefore, it is important to understand the internal structural changes and cell temperature distribution to improve safety, reliability and cycle life of batteries.

As noted in a number of publications [16], [18–20] an accurate measure of LIB internal temperature is one of the most effective parameter to determine overall performance [21]. In contemporary electric vehicles, temperature is often only measured at the module level at a subset of locations within the battery assembly. The main concern with this approach, is that significant changes in absolute temperature or the formation of temperature gradients within the battery will not be identified. This, in turn, may lead to faster degradation rates or the onset of thermal runaway [22,23]. Therefore, the inclusion of a robust temperature sensor that can monitor the internal cell temperature during operation is of high importance. This will eliminate the need for complex algorithms or models to estimate internal temperature distribution. Researchers have applied thermocouples [20,24–26], thermistor [18] and fibre Bragg grating [27–29] inside various types of cells to monitor the internal temperature. However, such methods are limited by the spatial measurement point due to non-uniform internal temperature distribution.

Mechanical damage in an electrode is driven by the structural deformation that are induced during cycling [30]. There are numerous theoretical and computational efforts in the literature devoted to understand the strain in graphite anode at the particle level [7,31,32] and the electrode level [11,17,30,33]. Particle level simulation considered the stress of graphite particles raised from the lithium ion concentration gradient from the graphite particle surface to its interior. However, the complexity of the internal cell structure composing of porous and composite elemental structures creates difficulties in achieving accurate models and parameter predictions. Electrode level stress measurements were most demonstrated by a cantilever beam-bending method based on monitoring curvature of the substrate and calculated by the Stoney equation [34–36]. However, this method cannot provide detailed stress distribution but overall stress parallel to the substrate, with a complicated experimental cell setup incorporating an observational window. Ex-situ micro-Raman spectroscopy (MRS) demonstrated stress characterisation in static state during prolonged charge-discharge cycling based on the mapping of graphite particles [37–39]. Nonetheless, MRS cannot precisely monitor real-time stress evolution during cycling. Recently, Fibre Bragg grating (FBG) used as an implanted sensor demonstrated monitoring of local stress evolution of one electrode in real-time [27–29]. However, the FBG techniques are restricted in its number of sensing points, leading to a limited understanding of real-time distributed strain/stress evolution inside of the cell at different points.

In this study, we demonstrate how a Rayleigh scattering based distributed optical fibre can be employed to improve our understanding of the fundamental thermal and electrochemistry of LIB, by embedding a pair of sensors within the anode electrode. To the best of our knowledge, this is the first time that this innovative sensing technique has been reported for this application. This *in-situ* and *operando* characterisation techniques can provide valuable real-time information and insights on the interrelated effect of electrode mechanical degradation, structural evolution and electrochemical kinetics, which can help researchers understand battery process and design better battery systems.

2. Materials and methods

2.1. Rayleigh scattering based distributed fibre optic sensor (DFOS)

Herein we examine Rayleigh scattering based optical fibre sensors due to their high chemical stability and small diameters. Such fibres were embedded to the anode electrode of a prototype pouch cell to monitor the distributed strain and temperature in real-time during various operating conditions.

When an electromagnetic wave is launched into an optical fibre, the light will be redistributed by Rayleigh scattering [40,41]. If the local changes in temperature and strain are relayed to the optical fibres, the scattered signal in the fibre will be modulated by these physical parameters. As a result, by measuring changes in the modulated signal, it is possible to quantify local physical variables of temperature and strain. The desired features of Rayleigh scattering based fibre sensing technique allows distributed measurements with millimetre-scale spatial resolution and high measurement accuracy, making it a suitable solution for LIB *operando* and *in-situ* applications. A pair of DFOSs, a temperature-DFOS (T-DFOS) and a strain-DFOS (ε-DFOS), were deployed to measure and discriminate distributed temperature and strain. Since temperature and strain were measured simultaneously, thermal strain and mechanical strain of the anode can be derived and investigated in real-time for various different use cases. The conditions explored as part of this research include, but are not constrained too: LIB formation after manufacturer and prolonged electrical loading using a constant-constant (CC) and constant voltage (CV) profile to define LIB performance and degradation.

Coherent Optical Frequency Domain Reflectometry (C-OFDR), a type of Rayleigh scattering based DFOS, is performed to monitor distributed strain and temperature of the anode electrode. C-OFDR was selected due to its high spatial resolution (2.6 mm) measurement capability. The configuration consists of a main interferometer and an auxiliary interferometer, as shown in Fig. 1. The operation of the experimental set-up is explained below.

The main interferometer contains two optical couplers (OC1 and OC2), an optical circulator (CIR), two polarisation controllers (PC1 and PC2), a fibre under test (FUT) and a polarisation beam splitter (PBS). The auxiliary interferometer includes two optical couplers (OC3 and OC4). The optical frequency of the output laser from the tuneable laser source (TLS) is tuned in time, the laser splits into two arms after passing through the OC0. Then the frequency tuning laser launched into the main interferometer splits into two portions at OC1: one (light a) enters the CIR, the PC1 and the FUT, the reference light (light b) enters the PC2. The spontaneous Rayleigh backscattering light in the FUT interferes with light b at the OC2. The interference light transmits to the PBS and then splits into two orthogonal polarisation components (P and S). P and S are detected by the photo detectors (PDs) and stored by the data

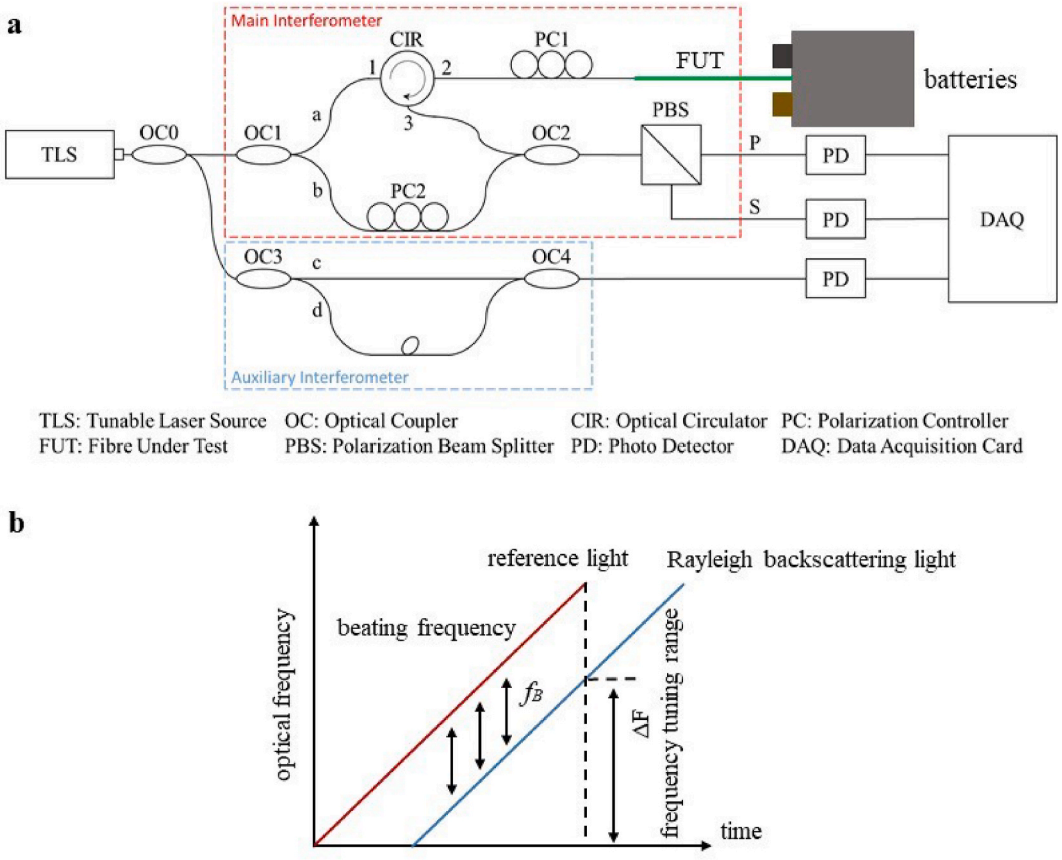

Fig. 1. a, Configuration of a Coherent Optical Frequency Domain Reflectometry (C-OFDR) system. **b**, Interference between Rayleigh backscattering light and reference light.

acquisition card (DAQ). In this way, polarisation has no effect on the value of Rayleigh backscattering amplitude. Meanwhile, the laser launched into the auxiliary interferometer splits into light c and light d, an interference between them occurs at the OC4, the interference light is employed as a trigger signal to mitigate the tuning nonlinearity.

By analysing the interference signal of the main interferometer, it can be found that a specific frequency f_B, named as the beat frequency, directly corresponds to a specific position (z) along the FUT. The spatial resolution Δz can be given as

$$\Delta z = \frac{c}{2n_g \Delta F} \tag{1}$$

where c is the speed of light in space, n_g is the group refractive index, ΔF is the frequency tuning range of the TLS. In known conditions, a stable and unique fingerprint Rayleigh backscattered spectrum (RBS) is acquired. The local RBS shifts in frequency when an variation in the environmental conditions occurs. The cross-correlation of the measurement RBS and the fingerprint RBS determines the local spectral shift $\Delta\nu$, which can reveal local information (e.g. temperature and strain) along the whole fibre by using proper calibration constants. A change in temperature or strain from the baseline condition results in a frequency shift in the spectrum of light scattered in the fibre. Changes in the local period of Rayleigh scattering cause temporal and spectral shifts in the locally-reflected spectrum, which can be scaled to form a distributed sensor. The strain response arises due to both the physical elongation and compression of the sensor, and the change in fibre index due to photoelastic effects [42]. The thermal response arises due to the inherent thermal expansion of the fibre material and the temperature dependence of the refractive index [42].

The optical fibre employed in this study is a polyimide coated, low bend loss, single mode fibre. The physical length and refraction index of the fibre are intrinsically sensitive to the measurement of both temperature and strain; therefore, the single-mode fibre sensor is used as the ε-DFOS. The ε-DFOS measures both strain and temperature simultaneously. The single-mode fibre housed loosely in a Poly-Tetra-Fluoro-Ethylene (PTFE) tube (jacket), to ensure minimum disturbance caused by the mechanical strain. The resultant measurement is solely a function of variations in temperature. As a result, this fibre is used as T-DFOS. The T-DFOS measures temperature only. Therefore, in order to capture distributed strain and temperature information respectively, a pair of ε-DFOS and T-DFOS were placed parallel and side by side to the subject under test, followed by temperature compensation of strain calibration.

2.2. Measurement principle

The shift in the spectrum of light scattered in the ε-DFOS in response to strain and temperature is analogous to a shift in the spectral shift, $\Delta\nu_{\varepsilon-DFOS}$:

$$-\frac{\Delta\nu_{\varepsilon-DFOS}}{\nu} = K_T \Delta T_{measured} + K_\varepsilon \varepsilon_{measured} \tag{2}$$

Where ν is the mean optical frequency, K_T and K_ε the temperature and strain calibration constants, $\Delta T_{measured}$ and $\varepsilon_{measured}$ are the measured temperature change and strain. The value of K_T and K_ε are dependent on the dopant species and concentration in the core of the fibre [43].

This thermal response arises due to the inherent thermal expansion of the fibre material and the temperature dependence of the refractive index. In the absence of any mechanical strain, the frequency shift, $\Delta\nu_{T-DFOS}$, due to temperature change ΔT is defined as:

$$-\frac{\Delta\nu_{T-DFOS}}{\nu} = K_T \Delta T_{measured} \tag{3}$$

The default values for these constants are set at common values for germanosilicate core fibres: $K_T = 6.45$ x 10-6 °C^{-1} and $K_\varepsilon = 0.780$ [40, 44]. The values for K_T and K_ε are dependent on the dopant species and concentration in the core of the fibre, but also to a lesser extent on the composition of the cladding and coating. Therefore, in the absence of strain, the temperature change can be defined as:

$$\Delta T_{measured} = -\frac{1}{K_T \nu}\Delta\nu_{T-DFOS} = C_T \Delta\nu_{T-DFOS} \quad (4)$$

Accordingly, the strain measurement can be compensated and calculated as follows:

$$\varepsilon_{measured} = -\frac{K_\varepsilon}{\nu}(\Delta\nu_{\varepsilon-DFOS} - \Delta\nu_{T-DFOS}) = C_\varepsilon(\Delta\nu_{\varepsilon-DFOS} - \Delta\nu_{T-DFOS}) \quad (5)$$

Assuming a scan centre wavelength of 1550 nm, the constants can be substituted in to yield the following temperature and strain conversion factors, which are after the compensation of the inherent thermal expansion of the optical fibre material through the calibration process, shown as (C_T and C_ε) respectively:

$$C_T = -0.801°C/GHz$$

$$C_\varepsilon = -6.67\varepsilon\mu/GHz$$

The strain response measured by the optical fibre, $\varepsilon_{measured}$, arises due to both the mechanical elongation of the subject under test (mechanical strain, ε_M), and the change due to thermal expansion of the subject under test (thermal strain, ε_T).

$$\varepsilon_{measured} = \varepsilon_M + \varepsilon_T \quad (6)$$

$$\varepsilon_T = k_{\varepsilon T} \times \Delta T \quad (7)$$

Where $k_{\varepsilon T}$ is the substrate coefficient of thermal expansion.

2.3. Calibration of ε-DFOS and T-DFOS

The strain and temperature calibration of the ε-DFOS and T-DFOS fibres were conducted in an Espec thermal chamber with temperature varying from 5 to 55 °C. The fibres, ε-DFOS and T-DFOS, were glued to a pure aluminium (99.996%) bar. The ε-DFOS and T-DFOS were placed closely to one another with a resistance temperature detector (RTD) mounted in close proximity. The strain sensitivity of the fibre was recorded using the thermal expansion of the aluminium bar. The coefficient of the thermal expansion at the aluminium bar is 23.6*10^{-6}/°C. For all the characterisation measurements presented in Fig. 2, tests were performed on at least three pairs of ε-DFOS and T-DFOS and repeated three times to allow statistical analysis of the results. The temperature and strain measurement accuracy are defined as ± 0.6 °C and ±30 με using the temperature and strain conversation coefficients C_T and C_ε respectively.

3. Experimental setup

3.1. Cell manufacture and instrumentation process

Fig. 3 presents the experimental set-up of a prototype pouch cell with an embedded pair of DFOSs, of which includes a T-DFOS and a ε-DFOS.

In order to measure the distributed strain of the anode, the ε-DFOS was bonded in the middle of the anode routing from the tab to the bottom of the cell (0–185 mm). The T-DFOS was placed between this anode and separator and alongside the ε-DFOS. The schematic of instrumented pouch cell with a pair of ε-DFOS and T-DFOS is shown in Fig. 4a and b. The pouch cell consists of seven layers of graphite anode and eight layers of nickel-manganese-cobalt (NMC) cathode, where the pair of DFOS are instrumented in the middle anode layer (e.g. layer 4). To ensure that the instrumentation process does not adversely impact LIB performance, a conventional cell and an instrumented derivative were electrically loaded for 100 cycles using a 1C constant-constant (CC) constant voltage (CV) profile. Fig. 4c compares the capacity fade for the 100 cycles of instrumented (with DFOSs) and non-instrumented cell (without DFOS). As it can be seen, there is negligible difference in cycle life.

3.2. Battery test procedure

The real-time experimental setup is shown schematically in Fig. 4b and consists of three parts: (1) the instrumented pouch cell with the pair of DFOSs; (2) the pair of DFOSs connected to the C-OFDR analyser and finally (3) the cell connected to the Bitrode cycler and placed in the Espec thermal chamber.

The Objectives of the experimental research are summarised below.

- To obtain the thermal expansion coefficient of anode electrode.
- To undertake in-situ monitoring of the SEI formation and irreversible anode structural deformation
- To quantify the relationship between anode strain and battery SoC during electrical cycling
- To quantify the relationship between anode strain and battery SoH during electrical cycling

To meet these objectives a programme of four experiments has been

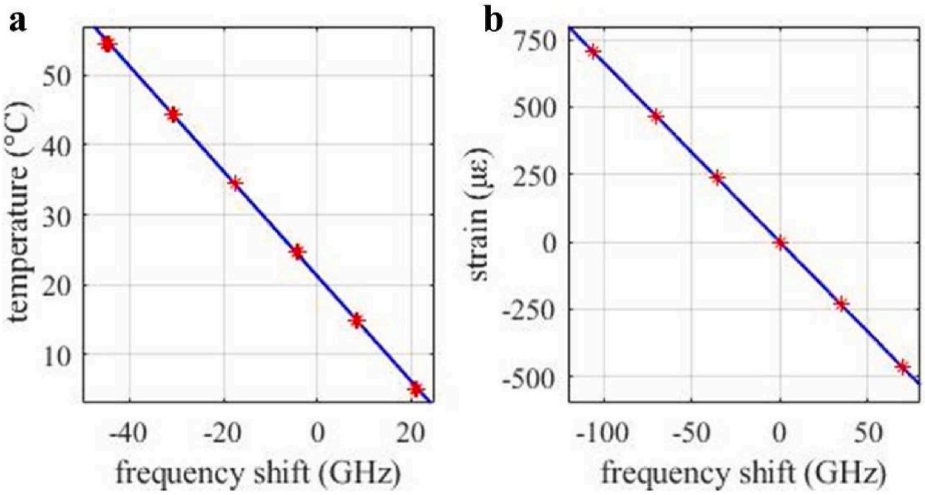

Fig. 2. Temperature (**a**) and strain (**b**) as a function of frequency shift with a linear fit applied to 100 raw experimental measurements.

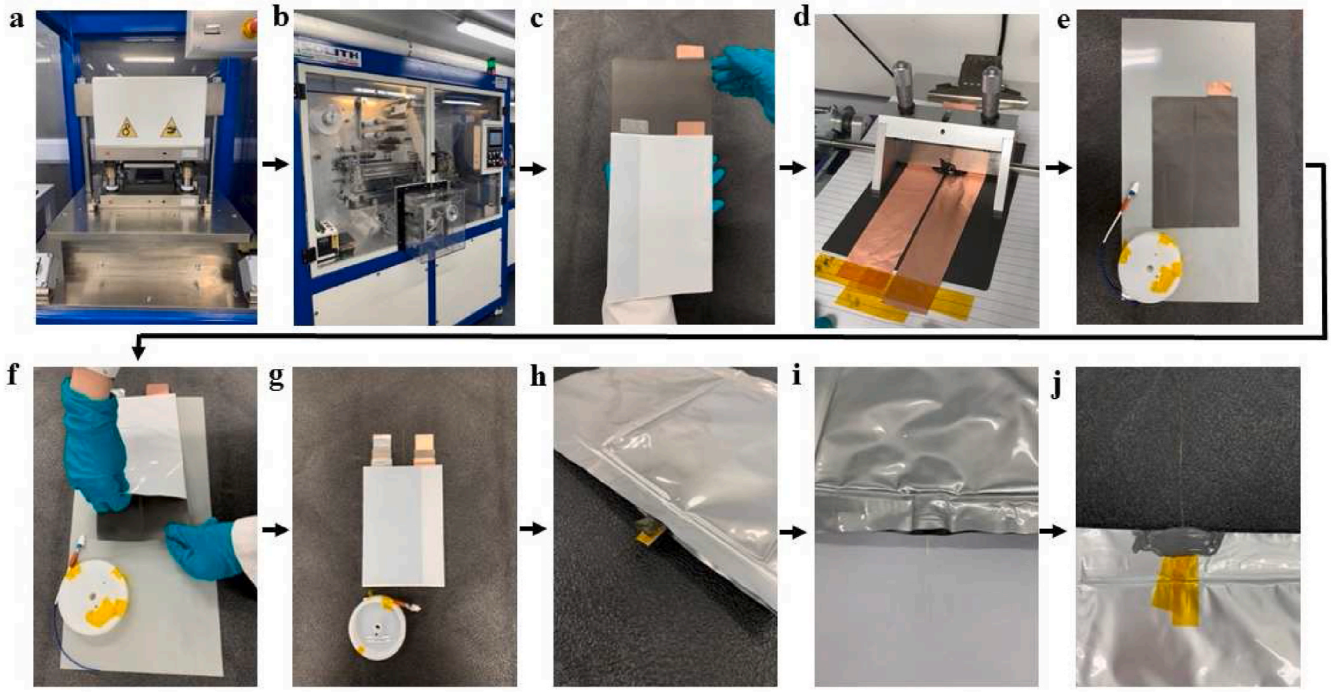

Fig. 3. Pouch cell instrumentation process: **a**, cutting the electrode. **b**, Stacking the electrode. **c**, the central anode electrode layer of the overall stack is carefully removed by sliding it out of the stack assembly. **d**, Bonding the ε-DFOS. the ε-DFOS is then bonded to the removed anode layer using a slurry paste of the same composition as the active material. The size of the double-sided coated anode electrode used was 185 mm in length and 130 in width. The anode slurry consisted of ~92% active material containing graphite, carbon black, and polyvinylidene difluoride (PVDF) in N-methyl-2-pyrrolidone (NMP) solvent. PVDF binder solution was first prepared by dissolving PVDF 5130 powder into the NMP solvent using an overhead high speed homodisperser (Model 2.5, PRIMIX) with a gradual increase in speed for 2 h. This solution was then mixed in a centrifugal mixer (Thinky mixer ARE-250) at 2000 rpm for 5 min. The final concentration of PVDF in NMP was ~8% wt. The slurry was then coated onto copper foil (10 μm, Oak Mitsui, electrodeposited) using a draw-down coater (RK Instruments Ltd) with a micro-meter-controlled spreading blade (K control coater Model 101, RK Print) with a blade gap of 300 μm **e**, The coated copper foil was dried on a hot plate set to 80 °C to evaporate the solvent for 15 min **f**, - Once dried, the ε-DFOS instrumented anode was placed back in its position within the stacked electrodes. **g**, The tabs were then welded and the T-DFOS was placed next to the ε-DFOS by fixing the two ends with tension. The current collectors for the cathode nickel-manganese-cobalt (NMC) and the anode graphite electrodes were aluminium and copper foils, respectively. **h** and **i**, Foam tape was employed to protect the ε-DFOS and T-DFOS as the pouch cells was sealed using a SOLITH sealing machine. **J**, Once sealed a non-electrolyte reactive Permabond adhesive was used to seal the protector inlet. Finally, the pouch cell was filled with electrolyte composing of a mixture of ethylene carbonate and ethyl methyl carbonate (3/7 vol ratio, respectively) containing 1% wt vinylene carbonate and 1 M LiPF6 using the SOLITH vacuum electrolyte filler.

derived. These are detailed below.

The first experiment was to obtain the thermal expansion of the anode electrode, by placing the instrumented cell into a thermal chamber, altering the chamber temperature from 10 °C to 40 °C and measuring the temperature and strain of the anode electrode.

In the second experiment, the electrometrical performance of the instrumented pouch cell was tested during formation and CC-CV repeated cycling at 25 °C ambient temperature controlled by the Espec thermal chamber. For the formation procedure, it commenced with a 30-min rest, followed by C/10 A CC charge phase until a cut-off voltage of 4.2 V was reached, then the cell was held at 4.2 V until the charge current reduced below C/20 A at which point the cell was allowed to rest for 5 h. For discharge, a C/10 A CC current was applied to discharge the cell until a cut-off voltage of 2.5 V was reached.

In the third experiment, the cell was cycled five times using a 3C CC-CV charge with a 4.2 V cut-off voltage, followed by 3C CV discharge phase to a lower bound voltage of 2.5 V, followed by a 30 min rest. In the fourth experiment presented in this work, the cell was rested for 3 h and then cycled using 3C CC-CV for charging and 3C CC for discharging for 25 repeated cycles with a 4.2 V cut-off voltage for charge and 2.4 V for discharge.

4. Results and discussion

4.1. Thermal and mechanical strain discrimination

Structural deformation of the anode during electrical cycling arises from two origins: thermal deformation and mechanical deformation. Thermal strain measures thermal deformation of the anode, which is the tendency of matter to change its physical shape in response to a change in temperature. Mechanical strain measures mechanical deformation, which is the physical transformation of a material from one configuration to another. In this study, mechanical strain refers to structural change that arises from the intercalation and de-intercalation of lithium with anode and SEI growth. Simultaneously, thermal strain results from thermal expansion of the anode due to changes in temperature as a result heat generation within the cell. By placing the instrumented cell into a thermal chamber, altering the chamber temperature from 10 °C to 40 °C, with 3 °C/min ramping rate, and measuring the temperature and strain of the anode electrode in real time, with 3 °C/min ramping rate, the thermal expansion coefficient of the anode can be derived by mathematically fitting the measured temperature and strain data points from the pair of DFOSs. With the assumption that the initial structure of anode is free from mechanical stress and thus deformation, at 25 °C, the thermal expansion coefficient of the anode was calculated to be 29.8 με/°C. This result is shown graphically in Fig. 5. Within this context, positive strain indicates expansion whereas negative strain implies shrinkage or compression of the anode material.

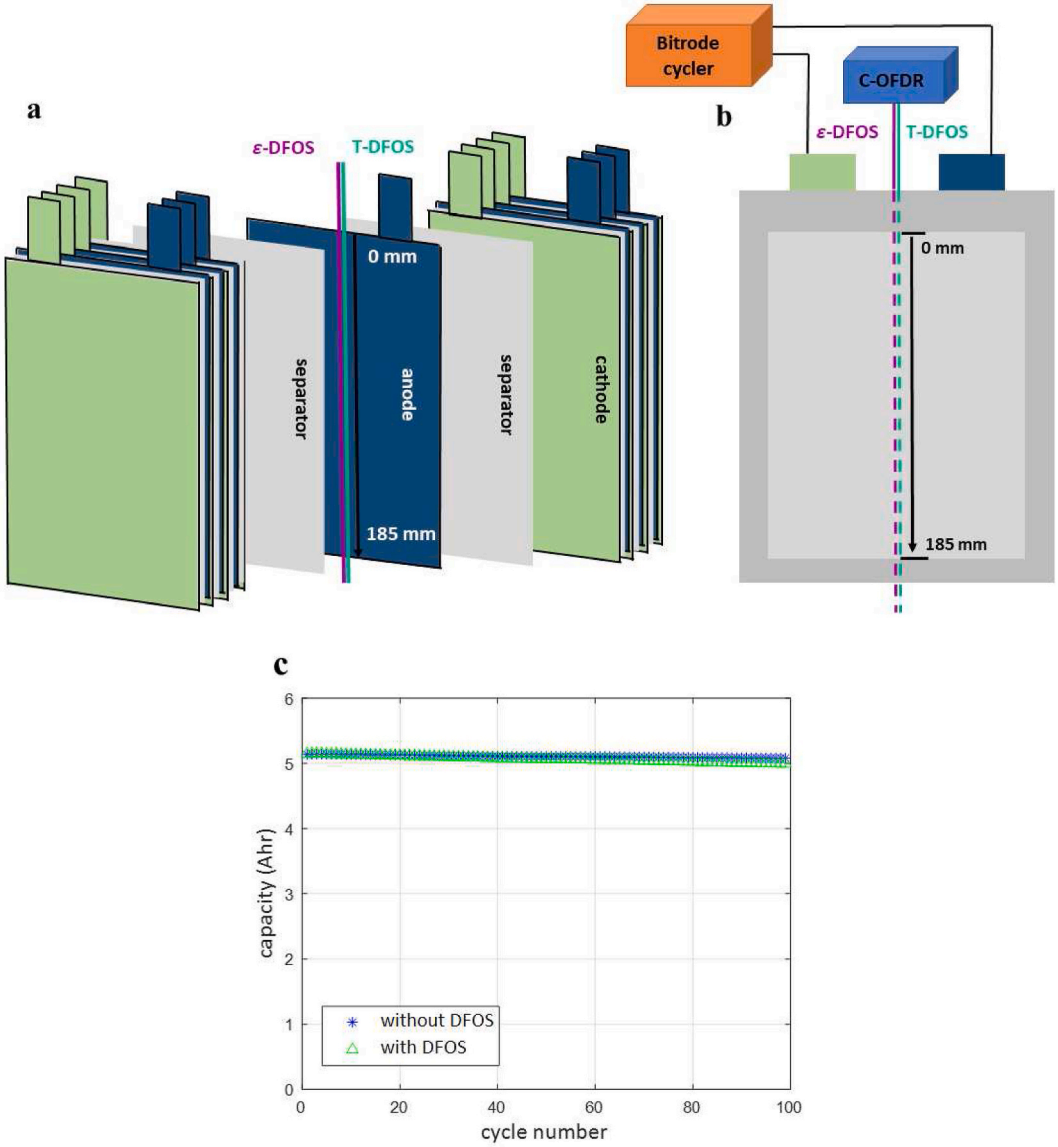

Fig. 4. **a**, Schematic of the ε-DFOS and T-DFOS instrumented the pouch cell. **b**, Schematic of the testing system, the instrumented pouch cell connected to the Bitrode cycler and the pair of DFOSs connected to the Coherent Optical Frequency Domain Reflectometry (C-OFDR). **c**. Battery performance unaffected by DFOSs by cycling at 1C for 100 cycles in a 25 °C ambient temperature.

4.2. Irreversible anode strain and SEI formation

It is widely known [45,46] that the formation of the SEI takes place on the surface of graphite electrodes due to the instability of the liquid electrolytes used at the operating potentials of the anode. The SEI layer acts as a passivating film to prevent any further excessive electrode-electrolyte side and therefore, playing a major role in determining the battery's electromechanical performance, including reversible and irreversible capacity and cycle life [47,48]. As highlighted within [45], a deeper understanding of SEI formation is important and could be underpin future innovations in cell design, battery manufacture and the design of algorithms to manage and extend battery life. Herein, the variation of cell voltage and current evolution alongside cell strain and temperature during the first formation cycles are monitored, as shown in Fig. 6. Non-uniform temperature distribution is observed across the cell from the cell tab to the bottom of the cell, detecting higher temperatures closest to the tab locations as illustrated in Fig. 6d. The measured strain distribution is uniform during the formation process, in which the area near the bottom of the cell experiences a higher expansion during charging compared with the area near the tab shown in Fig. 6b. It is observed that the measured strain of the anode rises during the first constant current charging step, indicating the swelling of the anode electrode during initial lithiation. During cell discharge, the strain decreased gradually to 2.5 V, signifying that as the anode de-lithiates, it reduces in size. Since temperature and strain distribution are measured simultaneously, the mechanical strain distribution can be calculated using equations (6) and (7). The mechanical strain distribution is dominated by the measured strain distribution format due to low temperature variations during cell formation.

As shown in Fig. 6f, the mean temperature (average of the distributed temperature measurements over the fibre length) increased by 2.7 °C during cell charge and remained constant until the voltage reaches a value of 4.2 V. As the cell undergoes a constant current discharge, the mean temperature variation was less than 1 °C until the voltage varied from 3.4 V to 2.5 V, where the mean temperature increased by 0.6 °C. The mean measured strain was found to be higher than the mean mechanical strain and follows the same trend resulting from low temperature variation during formation charge and discharge steps illustrated

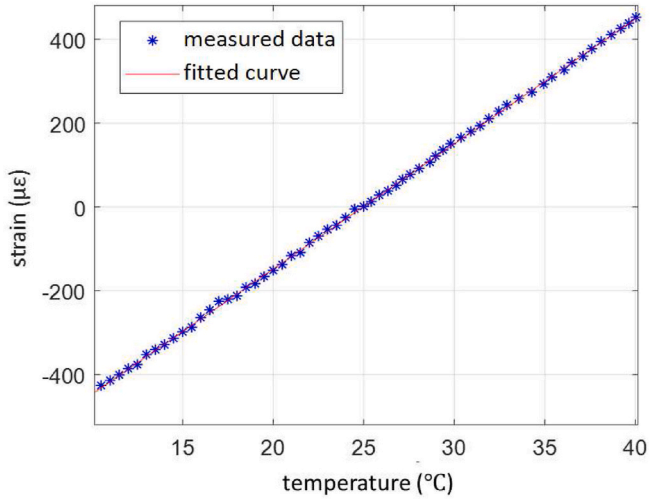

Fig. 5. Temperature and strain measured by setting the chamber temperature ranging from 10 °C to 40 °C.

in Fig. 6e.

By extracting the distributed strain obtained after the first electrochemical cycling from the initial distributed strain before formation, the irreversible distributed strain of the anode is calculated and exhibited in Fig. 6g. It is observed that the near top, middle and near bottom sections of the anode swell, but at the same time, the sections between them, the top edge and bottom edge experience mechanical compression after formation. Irreversible anode structural deformation was observed during the formation cycle, which based on [11,49,50], is attributed to irreversible expansion of the graphite particles and solvated lithium-ion co-intercalation.

4.3. Anode strain and SoC

The distributed strain and temperature characteristics of graphite anode undergoes 5 consecutive cycles composing of 3C CC-CV charging and 3C CV discharging cycles. For reference the last three cycles are depicted in Fig. 7. Assuming that the strain at 35 °C before the third charge is zero, the measured strain and temperature were observed to be non-uniformly distributed along the fibre from the tab to the bottom region of the cell, where the measured strain and temperature evolution follow a similar pattern during these three repeated cycles. The temperature gradient measured as the difference between maximum and minimum temperature along the fibre peaked at 7.9 °C during the first discharge of the three repeated cycles. The strain gradient measured as the difference between maximum and minimum strains along the fibre reached 189 με during the first charging step. By extracting mechanical strain from measured strain, the mechanical strain distribution is illustrated in Fig. 7c, in which the mechanical strain has an opposite trend compared with the measured strain due to the high temperature variation. The distributed mechanical strain increases during lithiation and reduce during de-lithiation, which corresponds to lithium-ion intercalation and de-intercalation respectively. These results indicate that the thermal and mechanical response of the anode graphite vary spatially and temporally along the electrode material during the 3C lithiation and de-lithiation.

During discharge, both measured strain and temperature increase and reach a maximum mean expansive strain (253με) and temperature (44.5 °C) at the end of discharge. This is highlighted in Fig. 7e and f. Both measured strain and temperature decrease during rest and reduce with a slower gradient during the CC-CV charging step. On the contrary, the mean mechanical strain increases during lithiation and reduces during de-lithiation. This result implies that the structural deformation of the anode is dominated by temperature rather than the lithium ion movement between crystal lattices during cycling further emphasising the impact of the high temperature variation cell performance and operating life.

In addition, by estimating the SoC calculated via column counting as the ratio of its current capacity to the nominal capacity and the corresponding instantaneous mean mechanical strain in the first cycle, the relationship between SoC and the mechanical strain are obtained and shown graphically in Fig. 7g. It shows that the anode reveals an extensive strain increase during a decreasing current (CV) charging. The high standard deviation obtained in the mean mechanical strain over the fibre length results from the non-uniformly distributed strain over the anode area from the tab to the cell bottom shown in Fig. 7g. By applying a linear fitting equation to the plot of SoC versus mean mechanical strain, a coefficient of 0.96 (με/SoC(%)) is calculated that define the gradient of the line. Applying this coefficient to the following two cycles, by comparing the calculated mechanical strain with the measured mechanical strain, ± 1.4 με fitting error was achieved.

4.4. Anode strain and aging

After the initial stabilisation experiment, the cell was allowed to equilibrate and then cycled at 3C CC-CV charging and 3C CC discharge for 25 repeated cycles. It is observed that the trend of mean measured strain is determined by the mean temperature shown as Fig. 8b and c respectively. It is noteworthy that due to the longer time associated with the CV stage of the charge profile, from the second to the tenth cycle, a gradual temperature increase is seen during both charging and discharging. From the tenth cycle, the temperature begins to stabilise as shorter CV charging steps are released. This reduction in CV time is caused by reduced capacity. By compensating for the temperature effect of anode expansion, the mechanical strain evolution reveals a repeatable response during lithiation and de-lithiation. The response translates to electrode swelling during lithiation and shrinking during de-lithiation.

By assuming the measured capacity in the first CC discharge step to be equivalent to the initial nominal capacity of the cell (100% SoH), the mean mechanical strain and capacity evolution during the 25 cycles (Fig. 8d) and SoH variation versus its corresponding mean mechanical strain (Fig. 8e) are obtained. Within this context, the value of SoH is taken as the ratio of the measured capacity to the nominal value. It reveals that the anode undergoes a compressive strain as SoH decreases from 100% to 47%. This is believed to be due to the high charge rates used which have a negative effect on the evolution of strain within the anode. The authors believe that a contributing factor to the compressive mean strain measured in this work is the reduction in SoH observed in the cells under test. As the cells are continually cycled and their capacity reduced, the period of constant-current discharge, combined with a constant cut-off voltage, implies that the graphite particles within the anode will become progressively more delithiated. Moreover, this variation in strain implies that the strain generated mainly occurs at during the early stage of cycling as shown in the Fig. 8. These results provide a further insight into understanding the degradation mechanisms of batteries as a result of electrode structural deformation.

5. Conclusions

Applying Rayleigh scattering based optical fibre sensing technique and the single mode fibre, we demonstrated simultaneous decoding of internal temperature and strain evolution of a pouch battery cell with advanced spatial and temporal accuracies, an achievement previously unattained by early efforts with optical sensing of batteries. Our approach is further extended in numerous ways: instantly extracting mechanical strain from measured strain by monitoring strain and temperature simultaneously, operando tracking of the SEI formation and the corresponding irreversible anode strain, in-depth assessment of anode structural deformation together with SoC and SoH from the first formation cycle and onwards, enabling the tracking of SEI formation,

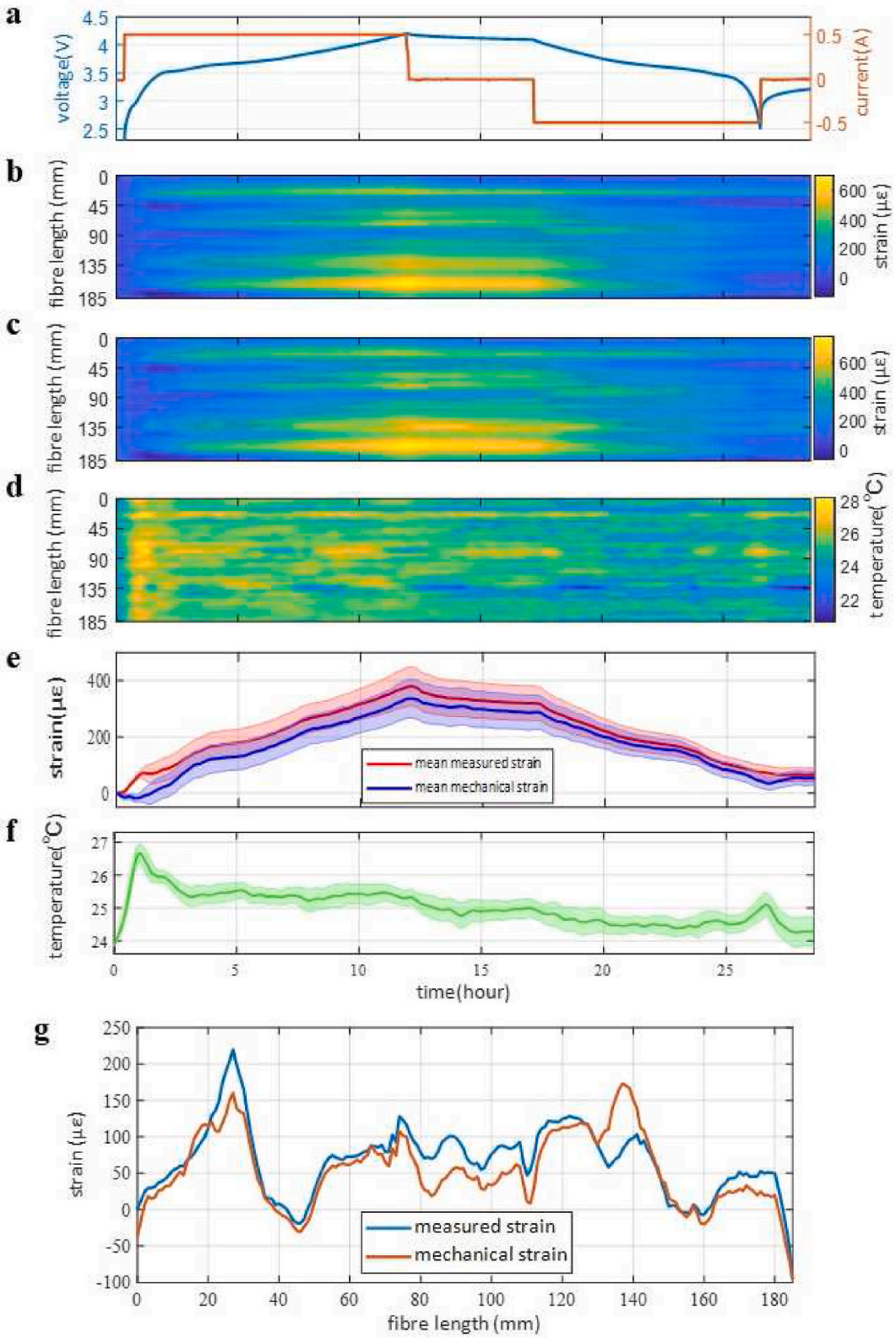

Fig. 6. Voltage and current (**a**), measured strain (**b**), mechanical strain (**c**), temperature (**d**), mean measured and mean mechanical strain over length (**e**), and mean temperature over length (**f**) evolution during first cycling at a constant rate of C/10. (**g**), Irreversible distributed measured strain and mechanical strain of anode after formation.

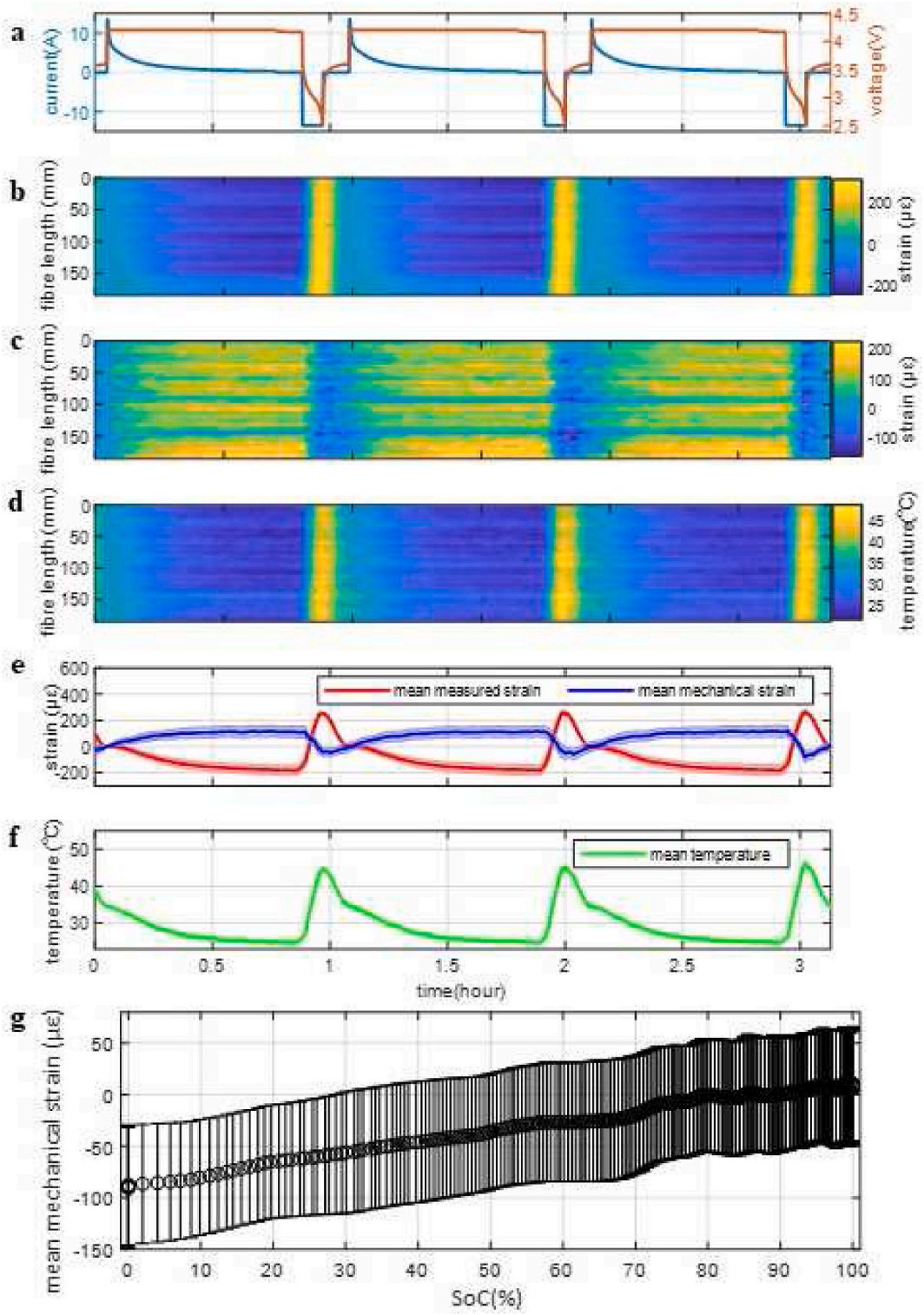

Fig. 7. Voltage and current (**a**), measured strain (**b**), mechanical strain (**c**), temperature (**d**), mean measured and mean mechanical strain over length (**e**), and mean temperature over length (**f**) evolution during 3C CC-CV charging and 3C CV discharging cycles. (**g**), SoC and the corresponding real-time mean mechanical strain with standard deviation of anode.

performance and cell lifetime.

Operando internal thermal and structural monitoring of a battery cell can provide valuable information to further understand the mechanism of battery performance degradation, emphasising the impact caused by electrode strain and temperature. Thus, this provides further characterisation of electrode materials which help with the optimisation of future battery designs. Moreover, electrode strain and temperature measures are vital for validation of battery stress and thermal models and thus for a reliable battery package design that is protected from fast performance degradation.

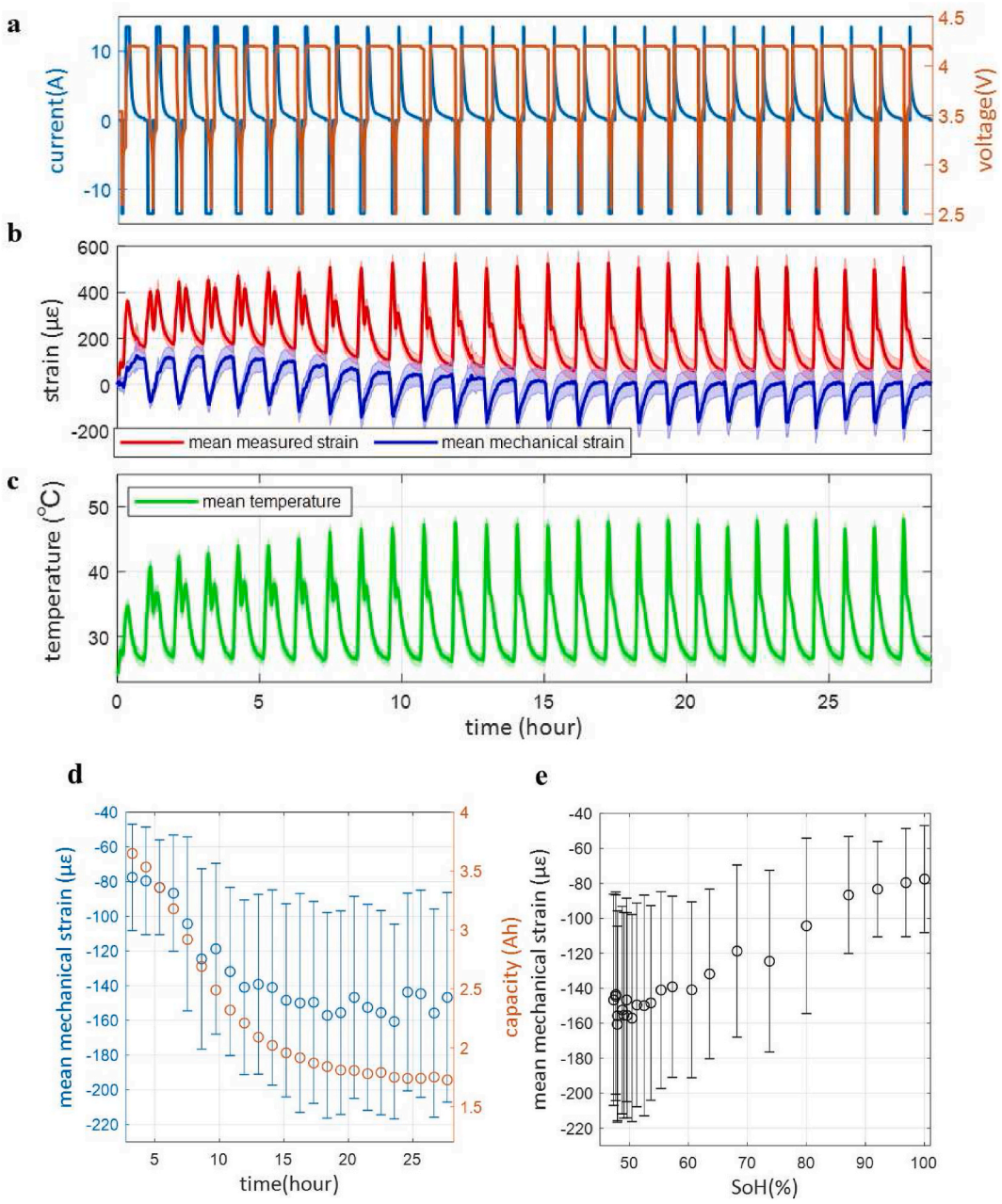

Fig. 8. Voltage and current (**a**), mean measured and mean mechanical strain over length (**b**), and mean temperature over length (**c**) evolution of 25 repeated cycles using 3C CC-CV charging and 3C CC discharging. (**d**), Mean mechanical strain and capacity evolution during cycling. (**e**), SoH and the corresponding real-time means mechanical strain with standard deviation of anode.

6. Future outlook

Further work is required to fully validate the accuracy and robustness of this embedded DFOS method relative to traditional state estimation techniques. In addition to NMC-graphite chemistry, the transferability of this approach to other cell formats and chemistries must be validated through additional experimentation. Aside from placing the fibres in a straight-line format in the centre of the cell, additional research should be undertaken to understand the optimal pattern for the fibre and the deployment approach to other components of the cell, such as the cathode, the electrical connections inside the cell and the cell's packaging or housing. particularly within large format pouch cells to improve the quality of the measurement data. This will help in understanding localised and non-uniform aging of batteries as it relates to special variations in heat generation and mechanical stresses. Moreover, this method can be coupled with imaging techniques which can provide capabilities that will allow researchers to monitor the formation and growth of cracks within electrode particles and the growth of dendrites in real-time due it's advanced resolution and accuracy. Real-time deployment of the measurement outputs may also be embedded within future BMS control systems to provide alternative methods of SoH estimation and the real-time estimation of internal temperature and mechanical stress as a function of SoC. Overall, the mathematical modelling, engineering and manufacturing communities will benefit from the measurement data using instrumented cells. The convergence of battery science and optical sensor engineering will be significant improvement of battery safety, reliability, performance and lifetime.

CRediT authorship contribution statement

Yifei Yu: Conceptualization, Methodology, Software, Validation, Formal analysis, Writing – original draft, Writing – review & editing. **Elena Vergori:** Software, Investigation, Data curation. **Faduma Maddar:** Writing – original draft. **Yue Guo:** Resources, Conceptualization. **David Greenwood:** Funding acquisition, Conceptualization. **James Marco:** Supervision, Project administration, Investigation, Writing – review & editing.

Declaration of competing interest

The authors declare that they have no known competing financial interests or personal relationships that could have appeared to influence the work reported in this paper.

Acknowledgement

This work was funded by the EPSRC (Engineering and Physical Sciences Research Council), grant reference EP/R004927/1, titled 'Prosperity Partnership'.

References

[1] M.M. Rahman, et al., Defect and structural evolution under high-energy ion irradiation informs battery materials design for extreme environments, Nat. Commun. 11 (2020) 4548.
[2] Z.P. Cano, et al., Batteries and fuel cells for emerging electric vehicle markets, Nat. Energy 3 (4) (2018) 279–289.
[3] J. ling Ma, et al., Prevention of dendrite growth and volume expansion to give high-performance aprotic bimetallic Li-Na alloy–O 2 batteries, Nat. Chem. 11 (1) (2019) 64–70.
[4] S. Li, et al., Mutual modulation between surface chemistry and bulk microstructure within secondary particles of nickel-rich layered oxides, Nat. Commun. 11 (1) (2020) 1–9.
[5] M.A. Hannan, et al., Toward enhanced state of charge estimation of lithium-ion batteries using optimized machine learning techniques, Sci. Rep. 10 (1) (2020) 1–15.
[6] F. Leng, C.M. Tan, M. Pecht, Effect of temperature on the aging rate of Li ion battery operating above room temperature, Sci. Rep. 5 (2015) 1–12.
[7] D. Lee, et al., Controlled swelling behavior and stable cycling of silicon/graphite granular composite for high energy density in lithium ion batteries, J. Power Sources 457 (February) (2020) 228021.
[8] A.J. Louli, L.D. Ellis, J.R. Dahn, Operando pressure measurements reveal solid electrolyte interphase growth to rank Li-ion cell performance, Joule 3 (2019) 745–761.
[9] J. Cannarella, C.B. Arnold, Stress evolution and capacity fade in constrained lithium-ion pouch cells, J. Power Sources 245 (2014) 745–751.
[10] Y. Ye, Y. Shi, N. Cai, J. Lee, X. He, Electro-thermal modeling and experimental validation for lithium ion battery, J. Power Sources 199 (2012) 227–238.
[11] N. Zhang, H. Tang, Dissecting anode swelling in commercial lithium-ion batteries, J. Power Sources 218 (2012) 52–55.
[12] N. Zhang, H. Tang, Dissecting anode swelling in commercial lithium-ion batteries, J. Power Sources 218 (2012) 52–55.
[13] A. Tomaszewska, et al., Lithium-ion battery fast charging: a review, eTransportation 1 (2019) 100011.
[14] B. Li, et al., Lithium-ion battery thermal safety by early internal detection, prediction and prevention, Sci. Rep. 9 (1) (2019) 1–11.
[15] J.P. Pender, et al., Electrode degradation in lithium-ion batteries, ACS Nano 14 (2) (2020) 1243–1295.
[16] L.H.J. Raijmakers, D.L. Danilov, F.J. Iek, D. Jülich, A review on various temperature-indication methods for Li-ion batteries, Appl. Energy 240 (July 2018) (2019) 918–945.
[17] V.A. Sethuraman, N. Van Winkle, D.P. Abraham, A.F. Bower, P.R. Guduru, Real-time stress measurements in lithium-ion battery negative-electrodes, J. Power Sources 206 (2012) 334–342.
[18] P. Wang, et al., Real-time monitoring of internal temperature evolution of the lithium-ion coin cell battery during the charge and discharge process, Extrem. Mech. Lett. 9 (2016) 459–466.
[19] G. Zhang, S. Ge, T. Xu, X.G. Yang, H. Tian, C.Y. Wang, Rapid self-heating and internal temperature sensing of lithium-ion batteries at low temperatures, Electrochim. Acta 218 (2016) 149–155.
[20] R.R. Richardson, P.T. Ireland, D.A. Howey, Battery internal temperature estimation by combined impedance and surface temperature measurement, J. Power Sources 265 (2014) 254–261.
[21] L. Lu, X. Han, J. Li, J. Hua, M. Ouyang, A review on the key issues for lithium-ion battery management in electric vehicles, J. Power Sources 226 (2013) 272–288.
[22] Q. Wang, P. Ping, X. Zhao, G. Chu, J. Sun, C. Chen, Thermal runaway caused fire and explosion of lithium ion battery, J. Power Sources 208 (2012) 210–224.
[23] H. Liu, Z. Wei, W. He, J. Zhao, Thermal issues about Li-ion batteries and recent progress in battery thermal management systems: a review, Energy Convers. Manag. 150 (May) (2017) 304–330.
[24] M. Xiao, S.Y. Choe, Theoretical and experimental analysis of heat generations of a pouch type LiMn2O4/carbon high power Li-polymer battery, J. Power Sources 241 (2013) 46–55.
[25] S. Chacko, Y.M. Chung, Thermal modelling of Li-ion polymer battery for electric vehicle drive cycles, J. Power Sources 213 (2012) 296–303.
[26] M.S.K. Mutyala, J. Zhao, J. Li, H. Pan, C. Yuan, X. Li, In-situ temperature measurement in lithium ion battery by transferable flexible thin film thermocouples, J. Power Sources 260 (2014) 43–49.
[27] M. Nascimento, et al., Internal strain and temperature discrimination with optical fiber hybrid sensors in Li-ion batteries, J. Power Sources (2019) 1–9.
[28] A. Raghavan, et al., Embedded fiber-optic sensing for accurate internal monitoring of cell state in advanced battery management systems part 1 : cell embedding method and performance, J. Power Sources 341 (2017) 466–473.
[29] A. Ganguli, et al., Embedded fiber-optic sensing for accurate internal monitoring of cell state in advanced battery management systems part 2: internal cell signals and utility for state estimation, J. Power Sources 341 (2017) 474–482.
[30] D. Liu, et al., On the stress characteristics of graphite anode in commercial pouch lithium-ion battery, J. Power Sources 232 (2013) 29–33.
[31] X. Li, et al., Design of porous Si/C-graphite electrodes with long cycle stability and controlled swelling, Energy Environ. Sci. 10 (6) (2017) 1427–1434.
[32] J.H. Lee, Y.M. Choi, U. Paik, J.G. Park, The effect of carboxymethyl cellulose swelling on the stability of natural graphite particulates in an aqueous medium for lithium ion battery anodes, J. Electroceram. 17 (2–4) (2006) 657–660.
[33] V.A. Sethuraman, M.J. Chon, M. Shimshak, V. Srinivasan, P.R. Guduru, In situ measurements of stress evolution in silicon thin films during electrochemical lithiation and delithiation, J. Power Sources 195 (15) (2010) 5062–5066.
[34] J.M. Rosolen, F. Decker, Stress in carbon film electrodes during Li + electrochemical intercalation, J. Electrochem. Soc. 143 (8) (2019) 2417–2421.
[35] K.Y. Chung, K.-B. Kim, Investigation of structural fatigue in spinel electrodes using in situ laser probe beam deflection technique, J. Electrochem. Soc. 149 (1) (2002) A79.
[36] H. Tavassol, M.K.Y. Chan, M.G. Catarello, J. Greeley, D.G. Cahill, A.A. Gewirth, Surface coverage and SEI induced electrochemical surface stress changes during Li deposition in a model system for Li-ion battery anodes, J. Electrochem. Soc. 160 (6) (2013) A888–A896.
[37] J. Lu, T. Wu, K. Amine, State-of-the-art Characterization Techniques for Advanced Lithium-Ion Batteries, March, 2017.
[38] Z. Zeng, N. Liu, Q. Zeng, S.W. Lee, W.L. Mao, Y. Cui, In situ measurement of lithiation-induced stress in silicon nanoparticles using micro-Raman spectroscopy, Nano Energy 22 (2016) 105–110.
[39] A.V. Diniz, N.G. Ferreira, E.J. Corat, V.J. Trava-Airoldi, Micro-Raman spectroscopy for stress analysis on large area diamond/Ti6Al4V electrodes, Diam. Relat. Mater. 13 (3) (2004) 526–532.
[40] M. Froggatt, J. Moore, High-spatial-resolution distributed strain measurement in optical fiber with Rayleigh scatter, Appl. Opt. 37 (10) (1998) 1735–1740.
[41] B. Lee, Review of the present status of optical fiber sensors, Opt. Fiber Technol. 9 (2) (Apr. 2003) 57–79.
[42] X. Bao, L. Chen, Recent progress in distributed fiber optic sensors, Sensors 12 (7) (2012) 8601–8639.
[43] A. Rogers, Distributed optical-fibre sensing, Meas. Sci. Technol. 10 (1999).
[44] S.T. Kreger, D.K. Gifford, M.E. Froggatt, B.J. Soller, M.S. Wolfe, High resolution distributed strain or temperature measurements in single- and multi-mode fiber using swept-wavelength interferometry, in: Opt. InfoBase Conf. Pap., January, 2006.
[45] A. Wang, S. Kadam, H. Li, S. Shi, Y. Qi, Review on modeling of the anode solid electrolyte interphase (SEI) for lithium-ion batteries, npj Comput. Mater. 4 (1) (2018).
[46] Y. Gao, et al., Low-temperature and high-rate-charging lithium metal batteries enabled by an electrochemically active monolayer-regulated interface, Nat. Energy 5 (7) (2020) 534–542.
[47] M. Broussely, et al., Main aging mechanisms in Li ion batteries, J. Power Sources 146 (1–2) (2005) 90–96.
[48] M. Dubarry, et al., Identifying battery aging mechanisms in large format Li ion cells, J. Power Sources 196 (7) (2011) 3420–3425.
[49] E.M.C. Jones, Ö.Ö. Çapraz, S.R. White, N.R. Sottos, Reversible and irreversible deformation mechanisms of composite graphite electrodes in lithium-ion batteries, J. Electrochem. Soc. 163 (9) (2016) A1965–A1974.
[50] X. Cheng, M. Pecht, In situ stress measurement techniques on li-ion battery electrodes: a review, Energies 10 (5) (2017) 1–19.